Energy Advances

Accepted Manuscript

This article can be cited before page numbers have been issued, to do this please use: S. Lavate and R. Srivastava, *Energy Adv.*, 2024, DOI: 10.1039/D4YA00417E.

ROYAL SOCIETY OF CHEMISTRY

rsc.li/energy-advances

View Article Online
DOI: 10.1039/D4YA00417E

Boosting Ethylene Yield via Synergistic 2D/0D Nanostructured VCu Layered Double Hydroxide/TiO_2 Catalyst in Electrochemical CO_2 Reduction

*Sneha S Lavate and Rohit Srivastava**

Catalysis & Hydrogen Research Lab, Department of Petroleum Engineering,

School of Energy Technology, Pandit Deendayal Energy University, Gandhinagar, Gujarat, India. 382426

E-mail of Corresponding Author: rohit.s@spt.pdpu.ac.in

Abstract

The electrochemical conversion of CO_2 into C_1 to C_2 hydrocarbon such as Methane and ethylene is a promising pathway towards to achieve net zero however due to high activation barrier for CO_2 it remains a big challenge. In this work, an effective strategy has been developed through the synthesis of a low-cost Vanadium and Copper based layered double hydroxide (LDH) decorated with TiO_2 nanoparticles (VCu LDH/TiO_2) as a highly efficient electrocatalyst for the electrochemical CO_2 reduction to ethylene. The structural and morphological study of the developed electrocatalyst was analyzed with the help of various analytical instruments such as X-ray diffractometer (XRD), Fourier Transform-Infrared (FT-IR), Scanning Electron Microscopy (FESEM), X-ray photoelectron microscopy (XPS) and Transmission Electron Microscopy (TEM) which confirmed the successful formation of VCu LDH/TiO_2. The electrochemical CO_2 reduction reaction (CO_2RR) study was performed in 0.1 M $KHCO_3$ using H-type cell and showed the formation of CO, H_2, CH_4, and C_2H_4 value added end products. The highest faradaic efficiency of 84% for C_2H_4 was obtained at -0.4 V vs RHE. The above results suggest that the VCu LDH/TiO_2 NPs electrocatalyst may be an excellent candidate for the CO_2 reduction and can be also utilized in wide range of energy conversion and storage applications.

Keywords: CO_2 Conversion, Electrocatalyst, LDH, Green fuels, Ethylene

1. Introduction

Carbon dioxide (CO_2) reduction creates a hope for climate change by making clean fuels and chemicals from CO_2. Since the advent of the industrial revolution, humanity has heavily relied on fossil fuels, resulting in substantial CO_2 emissions into the atmosphere. The rapid increase in CO_2 levels has led to a global temperature rise of approximately 2°C, posing a grave threat

View Article Online
DOI: 10.1039/D4YA00417E

to both human life and property. Nonetheless, it is worth noting that CO_2 possesses inherent value as a cost-effective resource known as a C1 molecule. This innovation could revolutionize the fossil fuel industry and make it more sustainable. It involves using electricity from renewable sources (like wind, solar, and hydro) to convert carbon dioxide, a greenhouse gas, into valuable fuels, alcohols, and chemicals commonly used in energy and chemical production. This process, called electrochemical CO_2 reduction, could help us achieve carbon neutrality and combat the harmful effects of climate change [1–4]. In this process, electrons serve as the primary agent for reduction, working alongside a proton source commonly found in water (H_2O). Electrochemical CO_2 reduction (CO_2RR) can be conducted at normal temperature and pressure, making it an environmentally sustainable reaction. The resulting reduction products, including carbon monoxide (CO)[5], formate[6], methanol[7], methane[8], ethylene[9], and ethanol[10], hold significant value as essential raw materials for both chemicals and fuels [11,12].

Out of the various products produced from the reduction of carbon dioxide, ethylene is one of the highly sought after due to its widespread industrial applications and massive market demand. Reports indicate that the global ethylene market is projected to experience significant growth, increasing from $190.29 billion in 2020 to $302.22 billion in 2025, with a compound annual growth rate (CAGR) of 7% [13–15]. Reducing CO_2 to ethylene is the most sought and valuable reduction product due to its great market demand. Ethylene is a key raw ingredient in the polymer, pharmaceutical, and high-tech industries. Additionally, ethylene can be used as a welding fuel or natural gas additive. Currently, ethylene is mostly produced by cracking non-renewable naphtha under high temperatures. The production process consumes energy and typically has a detrimental influence on the environment. CO_2RR is a sustainable and environmentally friendly method for selectively producing ethylene [16]. Hence, the electrochemical conversion of the greenhouse gas CO_2 into ethylene serve to reduce CO_2 emissions, enhance the atmospheric conditions, store renewable energy, and offers substantial economic advantages.

CO_2, an inert linear molecule with a robust C=O bond (750 kJ mol^{-1}), necessitates a high amount of energy for its electrochemical conversion. The conversion of CO_2 to multi-carbon (C_{2+}) hydrocarbons or oxygenates is a complex process involving multiple proton-coupled electron transfers (PCET), which can result in various reaction intermediates and products. This complexity often leads to a low selectivity for ethylene. Theoretical studies suggest that adjusting the stability of these intermediates is key to customizing the selectivity of CO_2RR [17–19]. Electrochemical CO_2 reduction reactions face problems such as high overpotential, low Faradaic efficiency, competition with HER in aqueous electrolytes, and poor product selectivity

View Article Online
DOI: 10.1039/D4YA00417E

[20]. Among the various CO_2RR catalysts, Ag, Au, Zn, Pd, and others, depending on their adsorption strength for C_1 intermediates, can either enhance CO_2-to-C_1 activity or lead to catalyst poisoning. On the other hand, copper (Cu) catalysts possess a unique electronic structure that promotes the formation of C_1 intermediates with moderate adsorption strength. This characteristic results in superior catalytic performance for CO_2-to-C_{2+} conversion [21]. Hence, Cu-based catalysts are considered the most promising catalyst for producing ethylene from CO_2RR. Furthermore, the easy and energy-efficient synthesis, multiple valence states, and complicated molecular chemistry of vanadium-based compounds have spurred a lot of interest in the development of vanadium-based materials like VO_2, V_3O_7, V_6O_{13}, V_2O_5, and metal vanadates. Vanadium oxides are abundant in a variety of crystalline forms and exhibit excellent specific capacity, energy density, and electrochemical properties, making them very attractive choices for cathode materials in lithium-ion batteries. Furthermore, these compounds have robust interactions with molecular and ionic species, endowing semiconductor materials with electrocatalytic and/or photocatalytic properties [22–24]. Titanium dioxide (TiO_2) is a cheap, widely available, and ecologically benign material with a variety of uses. Because of its high activity and sufficient stability, TiO_2 is widely employed in many different applications [25].

In CO_2 reduction, H coverage is crucial in the process of hydrogenation. Therefore, one possible tactic to encourage the synthesis of C_2 and crucial intermediate is to increase H adsorption on the catalyst surface. In fact, elements like Cr, Mo, V, W, and others that are close to the sixth subfamilies have a strong affinity for hydrogen. According to earlier studies, doping with vanadium or chromium oxide can speed up the kinetics of hydrolysis and produce hydrogen protons. Cu surfaces decorated with oxides or hydroxides have been shown in earlier studies to have a large affinity for H atoms and to accelerate H_2O dissociation, both of which can accelerate the hydrogenation process in CO_2RR [26]. Ganganahalli K. Ramesha and co-workers carried out studies to find out the catalytic effect of TiO_2 on CO_2 reduction through spectroelectrochemistry and product analysis. Active reduction sites have been discovered as Ti^{3+} species that are produced when negative potentials are applied to the TiO_2 layer. The first one-electron reduction step is facilitated by the binding of CO_2 to catalytically active Ti^{3+} and subsequent electron transfer. The findings demonstrate that the TiO_2 surface functions as an electrocatalyst by reducing the voltage needed to reduce CO_2 [27]. Haiying He et al. projected a 0.24 V drop in the reduction potential of adsorbed CO_2 on a (101) surface of TiO_2 compared to a CO_2 molecule in aqueous solution using first principles calculations. The monodentate and bidentate configuration of CO_2 with TiO_2 leads to charge transfer through hybridised orbitals, resulting in a decreased reduction potential [28] (Scheme 1).

View Article Online
DOI: 10.1039/D4YA00417E

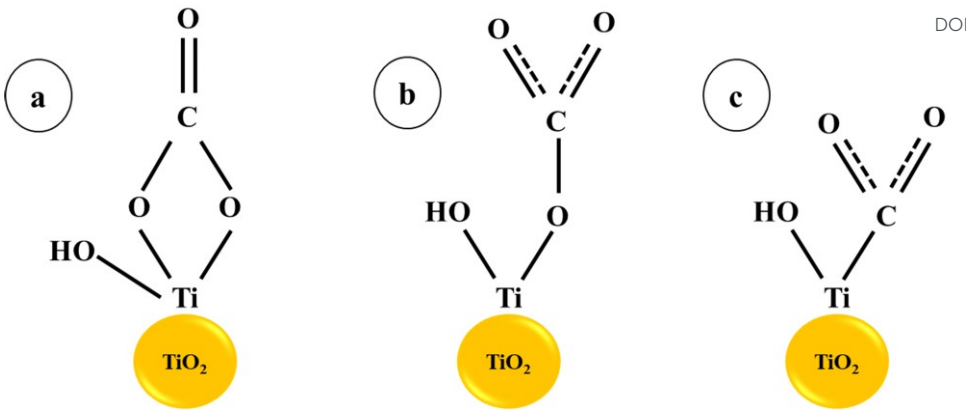

Scheme 1: CO_2 adsorption on TiO_2 surface: (a) Bidentate and (b) Monodentate interactions, (c) CO_2 adsorption at oxygen vacancy (or Ti^{3+}) site [28].

In the spheres of energy and environmental science, Layered Double Hydroxides (LDH) have recently emerged as a significant group due to their unique properties. Their importance in both theoretical investigations and practical applications has led to a growing interest in the development of methods for creating visibly active LDH as catalyst. This is a testament to the versatility and potential of LDH in these fields [29–31]. Layered Double Hydroxides (LDHs), also referred to as brucite-like materials, are a type of anionic clay that consists of cationic layers interspersed with anions. They have demonstrated significant potential and have been successfully used in various catalytic applications [32]. LDHs are utilized for wide applications such as sensors, sorbents, luminescence, water oxidation, water treatment, dye degradation, seawater electrolysis [33–37] etc. due to their versatile nature and facile synthesis. The structure of LDH is given as $[M^{II}_{1-x}M^{III}_{x}(OH)_2]^{Z+}(A^{n-})_{z/n}.mH_2O$, where M^{II} and M^{III} are divalent and trivalent metal ions, respectively, and (A^{n-}) are interlayered anions [38].

The main objective of this work is to develop a low-cost system for the reduction of CO_2 into various hydrocarbon fuels via electrochemical route. This paper reports the synthesis of 2D/0D VCu LDH/TiO_2 as a highly efficient electrocatalyst via simple and facile hydrothermal method for CO_2 reduction to value-added products. The VCu LDH/TiO_2 electrocatalyst exhibits excellent performance for CO_2RR in a conventional H-type cell with a C_2H_4 faradaic efficiency (FE_{C2H4}) of ~92% at -0.4 V vs RHE in 0.1 M $KHCO_3$ aqueous electrolyte along with CO and CH_4 with FE_{CO}=0.004% and FE_{CH4}=7.8%. The catalyst also revealed the highest partial current density of 377.8 mA/cm^2 at same potential.

View Article Online
DOI: 10.1039/D4YA00417E

2. Materials And Methods

2.1 Materials

Copper sulphate pentahydrate [$CuSO_4.5H_2O$, EMPLURA Merck, ≥ 98%], Vanadyl sulphate pentahydrate [$VOSO_4.5H_2O$, Kemphasol, 97.0%], Titanium Oxide [TiO_2, nanopowder, 21 nm primary particle size (TEM), ≥99.5%, Sigma Aldrich], Methanol [CH_3OH, Loba Chemie Pvt Ltd., AR grade 99.9%], Isopropyl alcohol [C_3H_8O, Loba Chemie Pvt Ltd., AR grade 99.5%] and Deionized water. All the chemicals were used without any further treatment.

2.2 Methodology

2.2.1 Synthesis of VCu LDH/TiO_2

In a typical synthesis, a 1:3 ratio of precursor salts of copper and vanadium were dissolved in deionised water. After dissolving the required quantity of TiO_2 nanopowder in deionised water, it was combined with the transition metal combination that was previously prepared. Following the homogeneity of the solution, the reaction mixture was heated for 17 hours at 160° C in a 100 ml Teflon autoclave made of stainless steel. A substantial amount of DI water and methanol were used to cleanse the resulting solution once the reaction mixture had cooled to room temperature. The product is cleaned and then vacuum-oven dried for an entire night at 80°C. After drying, a green finished product was produced, which was then put in a vial and preserved in a desiccator. The identical set of reactions were performed with reaction times of 3 and 6 hours and kept for later investigation.

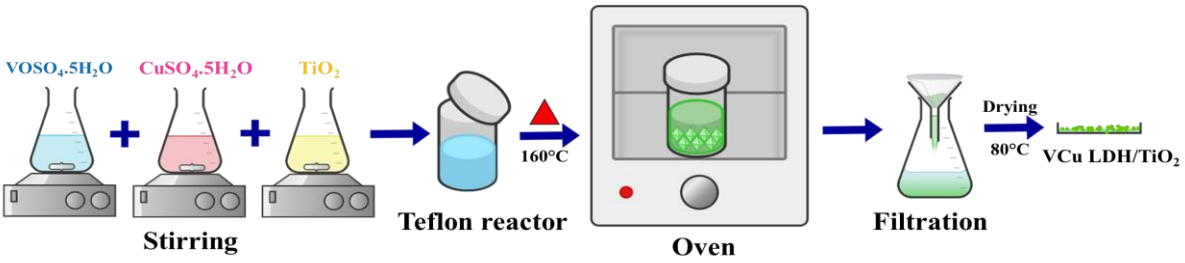

Figure 1: Schematic of synthesis of VCu LDH/TiO_2

2.2.2 Electrode preparation

For electrode preparation, a piece of carbon paper (1 cm × 2 cm) was taken and cleaned it with alcohol followed by drying it by solvent evaporation method. The catalyst ink was prepared by mixing 5 mg of as-prepared VCu LDH/TiO_2 catalyst with 1 mL of isopropyl alcohol and 10 µL of nafion solution within 2 ml vial. The mixture was further sonicated for 20 min to get a homogeneous catalyst ink suspension. Once the ink is homogeneously dispersed, 50 µL of ink was taken into the pipet and drop-casted on 1 cm^2 carbon paper (0.12 mg cm^{-2} mass loading). The obtained electrode was dried under vacuum in a desiccator prior to usage.

View Article Online
DOI: 10.1039/D4YA00417E

3. Instrumentation

Powder X-ray diffraction (PXRD) of VCu LDH/TiO_2 was conducted using Cu Kα radiation with XRD-D2 Phaser and LYNXEYE XE-T detector and λ= 0.15418 nm (Bruker Ltd Germany). Fourier Transformed Infrared Spectroscopy (FT-IR) was performed with Perkin Elmer Spectrum-2. X-ray photoelectron spectrometry (XPS) was recorded using Al Kα radiation (Thermo Fisher Scientific). The surface morphology of the catalyst was analyzed by Field Emission Scanning Electron Microscopy (FESEM, Zeiss ULTRA) with Energy Dispersive X-ray Spectroscopy (EDS). The High-Resolution Transmission Electron Microscopy (Talos Cryo-TEM) was used for the high-resolution micrographs along with Selected Area Electron Diffraction (SAED). Inductively Coupled Plasma Optical Emission Spectrometer (ICP-OES) analysis was performed by Model 7300:DV, Perkin Elmer. All electrochemical data were recorded with Gamry Interface-E0101 Potentiostat (Gamry Instruments). The end products of CO_2 reduction were analyzed using a Gas Chromatography (Chromatec Crystal 9000).

4. CO_2 Reduction Setup

For the CO_2RR, 0.1 M $KHCO_3$ was used as an electrolyte. A platinum foil and an Ag/AgCl was used as the counter and reference electrode, respectively. A gastight H-type glass cell, separated by Nafion (117) was used for the 3-electrode assembly for CO_2RR. Working electrode and reference electrode was placed in one compartment of H-cell and counter electrode in the other chamber as shown in Figure 2. The 75 mL of electrolyte solution was injected in each compartment of H-type electrochemical cell. Three electrodes in H-type cell were connected to the electrochemical workstation for controlling potential. The electrolyte was bubbled with CO_2 at 50 sccm using mass flow controller for 30 min towards CO_2-saturated 0.1 M $KHCO_3$ and maintained the CO_2 flow at 50 sccm throughout the following electrolysis.

The pH of the electrolyte, i.e. 0.1 M $KHCO_3$ saturated with CO_2 was determined using pH meter. All potentials measured against Ag/AgCl were converted to the Reversible Hydrogen Electrode (RHE) scale using following Equation 1,

$$E_{RHE} = E_{Ag/AgCl} + E^0_{Ag/AgCl} + 0.059pH \quad (1)$$

Where,

$E_{Ag/AgCl}$ = working potential

$E^0_{Ag/AgCl}$ = 0.197 at 25°C

View Article Online
DOI: 10.1039/D4YA00417E

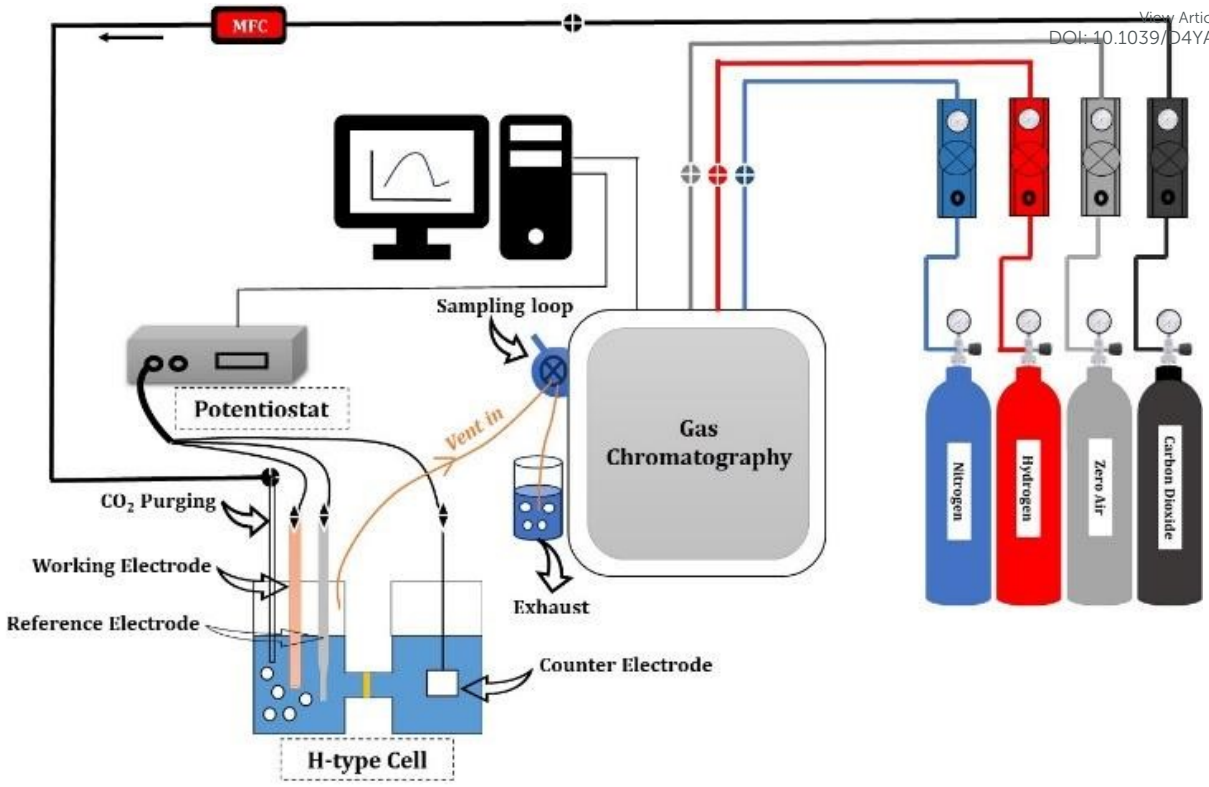

Figure 2: Schematic of CO_2 reduction experimental setup

5. Results & Discussions

5.1 X-Ray Diffraction

The XRD spectrum of VCu LDH/TiO_2, as depicted in the Figure 3, exhibit distinct peaks. These peaks, observed in the XRD spectrum of VCu LDH/TiO_2, are the result of a hydrothermal synthesis process with reaction time of 17 h. This indicates as synthesized catalyst exhibits considerable crystallinity, which can be attributed to the carefully calibrated hydrothermal reaction parameters that promote crystal growth. For comparison, the XRD of VCu LDH/TiO_2 synthesized at 3 h and 6 h is shown in Figure S3.

The XRD pattern for the VCu LDH exhibits several peaks, indicating a layered structure. The peaks observed at 6.69° (d = 1.32 nm), 7.54° (d = 1.17 nm), 23.23° (d = 0.38 nm), 25.52° (d = 0.35 nm), 27.26° (d = 0.33 nm), 30.64° (d = 0.29 nm), 32.69° (d = 0.27 nm), 33.54° (d = 0.27 nm), 40.91° (d = 0.22 nm), 42.25° (d = 0.21 nm), 47.73° (d = 0.19 nm), 52.22° (d = 0.18 nm), 54.01° (d = 0.17 nm), 59.74° (d = 0.16 nm), 60.79° (d = 0.19 nm), 70.75° (d = 0.13 nm), 76.23° (d = 0.12 nm) and 78.43° (d = 0.12 nm) can be attributed to diffraction planes of the layered double hydroxide structure following hkl planes (001), (003), (002), (006), (-202), (112), (021), (009), (-113), (-421), (313), (-204), (403), (-404), (332), (051), (043) and (405). The presence of these peaks confirms the successful synthesis of the VCu LDH material with a well-defined

View Article Online
DOI: 10.1039/D4YA00417E

layered structure as showed in our previous work [39]. The XRD matches with the JCPDS: 01-078-2077 corresponding to copper hydroxide vanadium oxide hydrate. The locations, strengths, and forms of the (003), (006), and (009) peaks, along with other peaks in the XRD pattern, provide researchers with important information about the interlayer spacing, the composition of the interlayer, the crystallinity, and the structural organization of the LDH material being studied [39].

Also, for TiO_2, visible peaks at 25.5° (d = 0.35 nm), 35.93° (d = 0.25 nm), 37.9° (d = 0.24 nm), 48.1° (d = 0.19 nm), 55.1° (d = 0.17 nm), 62.8° (d = 0.15 nm), 68.8° (d = 0.14 nm), 70.4° (d = 0.13 nm) and 75.1° (d = 0.13 nm) corresponds to JCPDS: 21-1272 [40] with hkl values (101), (103), (004), (200), (211), (204), (116), (220) and (215). The XRD plot in Figure 3 shows characteristic peaks of VCu LDH and TiO_2 merged together forming VCu LDH/TiO_2 heterostructure. The standard reference cards corresponding to VCu LDH and TiO_2 are attached in Figure S4.

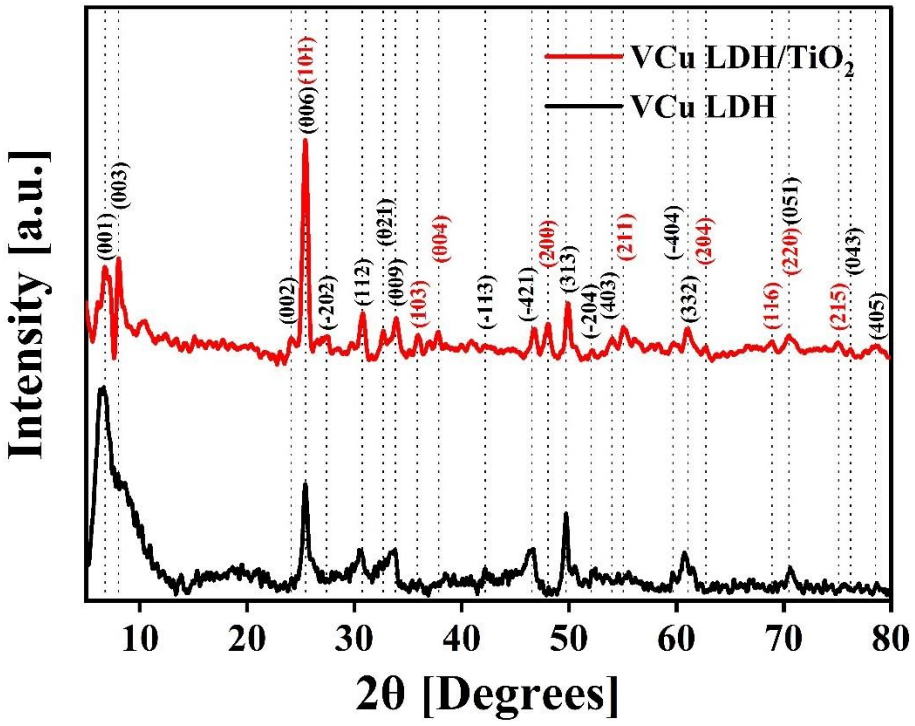

Figure 3: X-ray Diffraction Spectrum of VCu LDH (Black) and VCu LDH/TiO_2 (Red)

5.2 Field Emission Scanning Electron Microscopy (FESEM)

The surface morphology of the catalyst is seen by FESEM. The synthesized catalyst showed uniform flower-like morphology which is attributed to VCu LDH [39] with TiO_2 nanoparticles

View Article Online
DOI: 10.1039/D4YA00417E

decorated on the surface of the LDH flower. The FESEM images of VCuLDH/TiO_2 at were obtained at different resolutions of 10 µm, 2 µm, 1 µm and 200 nm are shown in Figure 4 below. The average thickness of the VCu LDH is ~18 nm whereas the TiO_2 nanoparticles of ~21 nm was used for the synthesis. When the reaction was carried out at 3 h and 6 h, there is no uniform flower-like morphology have been observed in the FESEM images (Figure S2). Therefore, catalyst synthesized at 17 h of reaction time was carried forward for further characterizations and analysis. The uniform distribution of the elements V (green), Cu (purple), Ti (blue) and O (red) has been observed in the Figure 4 below.

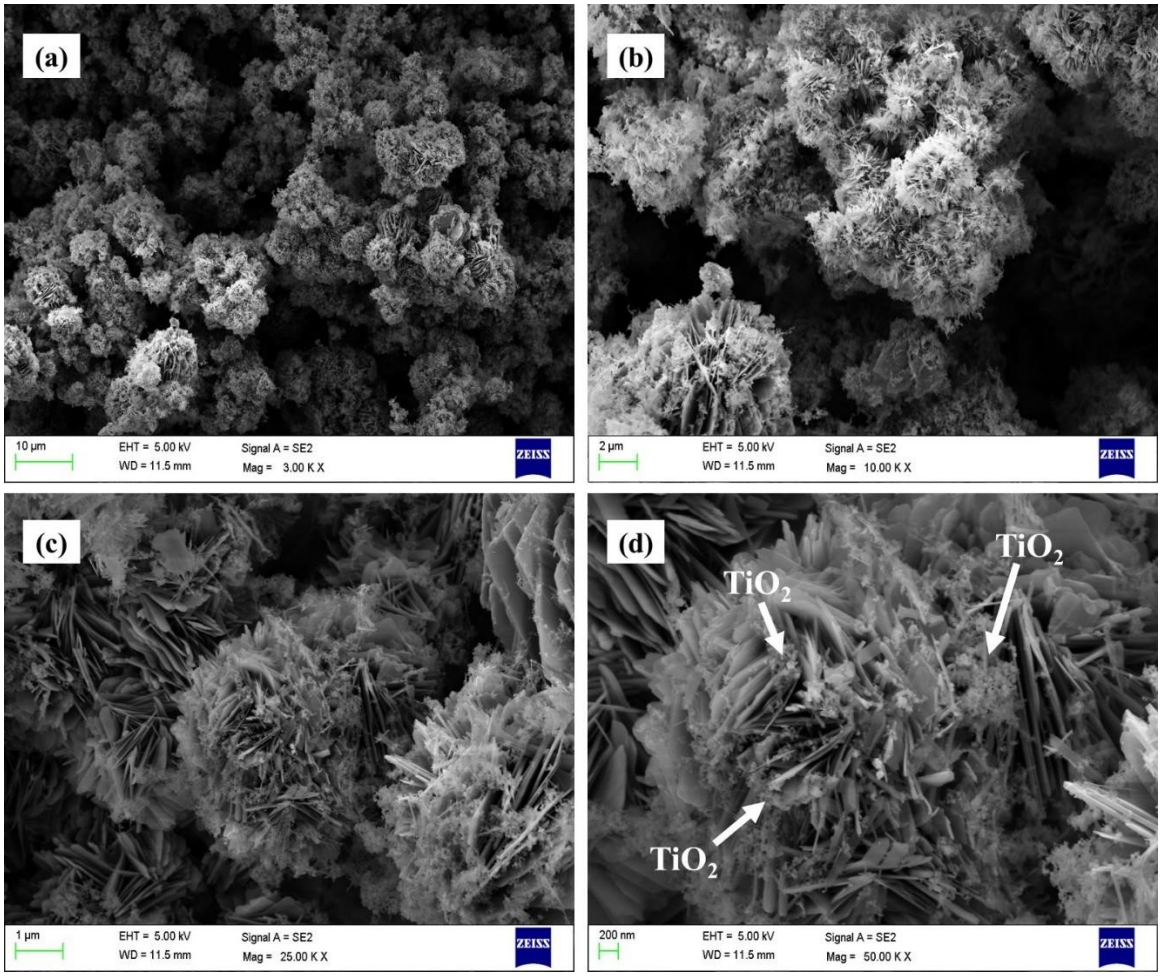

Figure 4: Field Emission Scanning Electron Microscopy images of VCu LDH/TiO_2 at different resolutions (a) 10 µm, (b) 2 µm, (c) 1 µm and (d) 200 nm

5.3 Fourier Transformed Infrared Spectroscopy (FT-IR)

The FT-IR spectrum of VCu LDH/TiO_2 are shown in Figure 5. The water molecules in the interlayer and the O-H group stretching vibrations of the hydroxide layers are linked to the wide absorption band in the 3600-3100 cm^{-1} area. The bending vibration of the interlayer water can be attributed to the band at around 1629 cm^{-1}. The M-O and O-M-O (M-V, Cu, Ti) stretching

vibrations are responsible for the peaks that are located below 800 cm^{-1} [41]. The development of LDH/TiO_2 as a composite is confirmed by the FTIR.

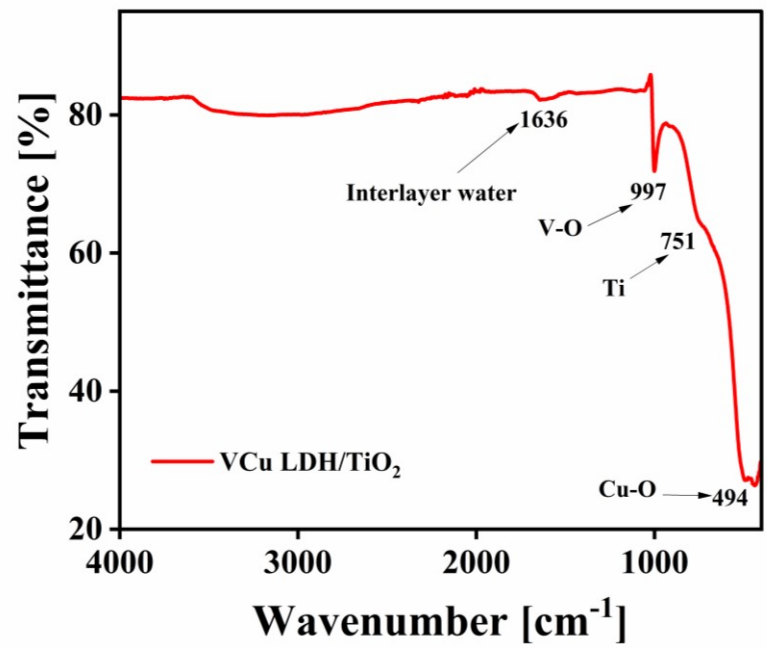

Figure 5: FTIR spectrum of VCu LDH/TiO_2

5.4 High Resolution-Transmission Electron Microscopy (HR-TEM)

Figure 6 is the high resolution-transmission electron microscopic images of VCu LDH/TiO_2 nanostructure at different resolutions (a) 50 nm, (b) 20 nm, and (c) 5 nm and (d) is the Selected Area Electron Diffraction (SAED). As seen in Figure 6 (a and b), the VCu LDH acts as the porous support for TiO_2 nanoparticles, forming 2D/0D hybrid nanostructure. This formation leads to increase in the more active sites for CO_2 adsorption. Figure 6 (d) shows the lattice fringes with the planes (003), (002) corresponding to VCu LDH and (101) corresponding to TiO_2 matching with XRD planes. The SAED pattern exhibits d spacing of 0.13, 0.17, 0.23 and 0.35 nm following (220), (211), (004) and (006) planes.

View Article Online
DOI: 10.1039/D4YA00417E

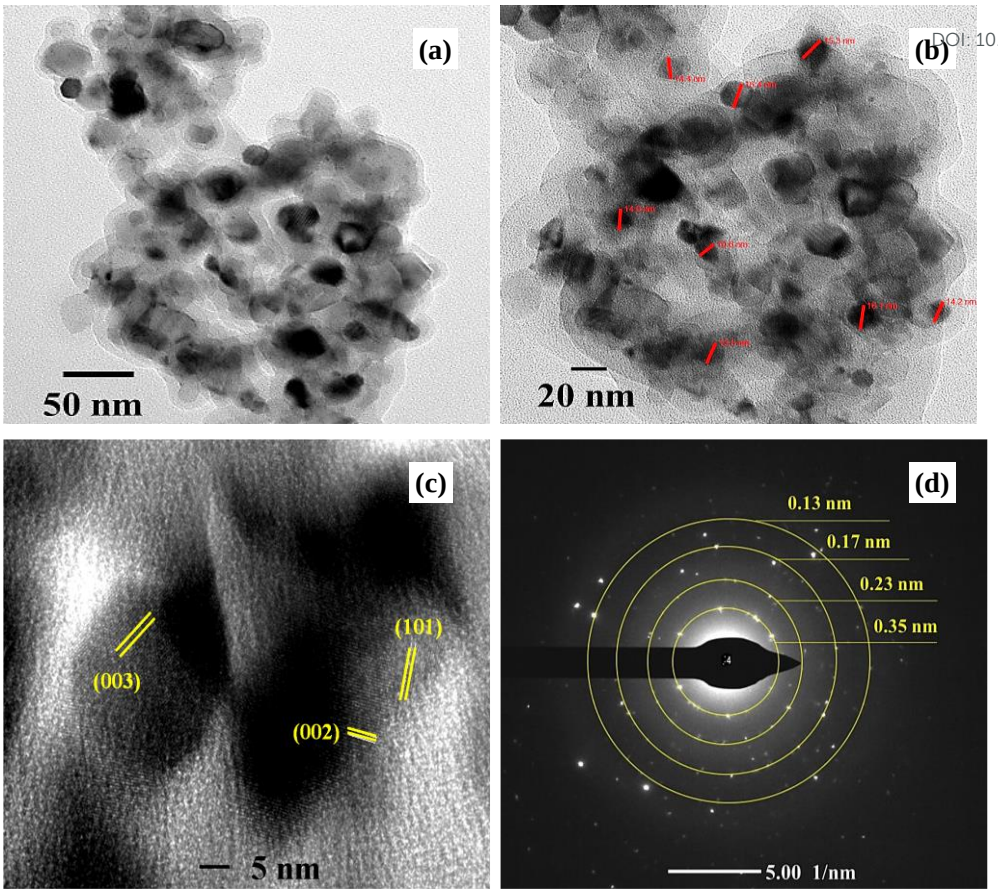

Figure 6: High Resolution Transmission Electron Microscopy Images of VCu LDH/TiO_2 at (a) 50 nm, (b) 20 nm, and (c) 5 nm. (d) SAED of VCu LDH/TiO_2.

5.5 X-ray Photoelectron Spectroscopy

Figure 7 (a) is full scan of VCu LDH/TiO_2 nanostructure. In Figure 7 (b-d), spectra of V 2p, Cu 2p and Ti 2p is shown respectively. The Figure 7 (e) is the O 1s spectrum. The binding energy at 514.3 eV attribute to V $2p_{3/2}$ spin corresponding to V(III) oxidation state. The weak binding energies at 929.0 and 948.6 of Cu 2p spectrum shows the presence of Cu(0) oxidation state. The peaks at 932.0 and 951.7 signifies the presence of Cu(II) oxidation state with Cu $2p_{1/2}$ spin. For Ti 2p, the binding energies at 455.7 and 461.5 eV is the attributed to Ti(III) oxidation state of VCu LDH/TiO_2 nanostructure. As the formula of LDH, $[M^{II}_{1-x}M^{III}_{x}(OH)_2]^{Z+}(A^{n-})_{z/n}.mH_2O$, where in our studies M^{II} corresponds to copper and M^{III} to vanadium.

View Article Online
DOI: 10.1039/D4YA00417E

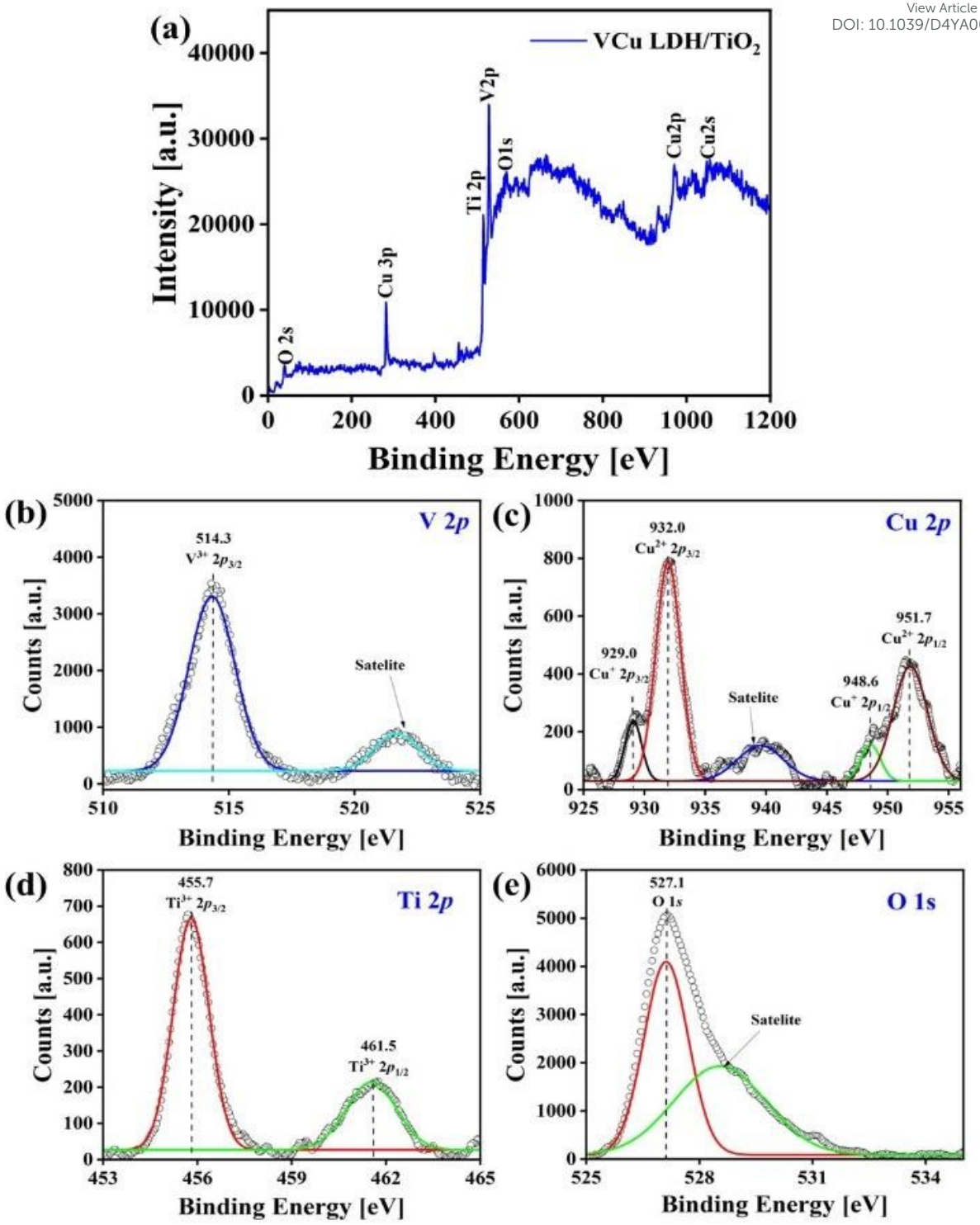

Figure 7: X-Ray Photoelectron spectrum of (a) full scan of VCu LDH/TiO_2, (b) V 2p, (c) Cu 2p, (d) Ti 2p and (e) O 1s.

5.6 Inductive Coupled Plasma-Optical Emission Spectrometer (ICP-OES)

The ICP-OES analysis is one of the major analyses to find out the exact concentrations of the elements present in any material. For analysis, the sample preparation was done by dissolving or digesting 4 mg of VCu LDH/TiO_2 catalyst with 50 ml nitric acid (HNO_3). The sample was

View Article Online
DOI: 10.1039/D4YA00417E

stirred and heated around 70°C till it gives transparent solution. From the final solution, 200 µl of sample was taken and added to 25 ml of milliQ water, further filtered by using a 0.45 mm nylon filter. The concentrations obtained were 0.042 mg/L for Copper (6.56 wt %), 0.277 mg/L for Vanadium (43.28 wt%) and 0.049 mg/L for Titanium (7.65 wt%).

5.7 Pathway of CO_2 Reduction to Ethylene

The CO_2RR process can be categorized into three distinct stages: the formation of a CO intermediate, C-C coupling, and hydrodeoxygenation of C_2 intermediates as shown in Figure 8. Drawing inspiration from the behavior of Cu clusters, the controllable hydrodeoxygenation process can also be achieved by introducing an additional active site on the Cu surface through bimetallic synergy, which can enhance the relative stability of oxygenated C_2 intermediates or the C-O bond [42]. Regarding the formation of the CO intermediate, CO_2 initially adsorbs onto the catalyst surface through strong M-O and M-C (M-Metal) bonds, causing the linear O-C-O bonds to bend due to the activation by the metals. Subsequently, the oxygen atoms in $*CO_2$ that are farther away from the metal surface become susceptible to attack by *H, leading to the generation of *COOH intermediate, followed by the formation of *CO species through the cleavage of a C-O bond. *CO is considered a crucial intermediate in the production of products with more than two electrons (>2e^-) from CO_2RR [18], owing to the similar product distribution observed in both CO and CO_2 reduction over Cu-based catalysts [43]. The *CO species, when adsorbed on the metal surface, can adopt different configurations, such as atop-, bridge-, and hollow-bound CO. In these configurations, the CO species interact with one, two, and more than three metal atoms, respectively [13,44,45]. The adsorption states of *CO play a significant role in determining the binding energy of *CO on the metal surface, which is vital for the subsequent hydrogenation process and influences the distribution of products [46,47]. This phenomenon elucidates the ability of Cu to catalyze the electroreduction of CO_2 to hydrocarbons and multi-carbon products. The pairing of $*CO_{\text{-atop}}$ and $*CO_{\text{-bridge}}$ species offers the potential for C_2 production through C-C coupling. On the other hand, $*CO_{\text{-hollow}}$, an inert species on the Cu surface, does not noticeably contribute to the formation of hydrocarbons due to its strong binding strength [44,45,48,49].

View Article Online
DOI: 10.1039/D4YA00417E

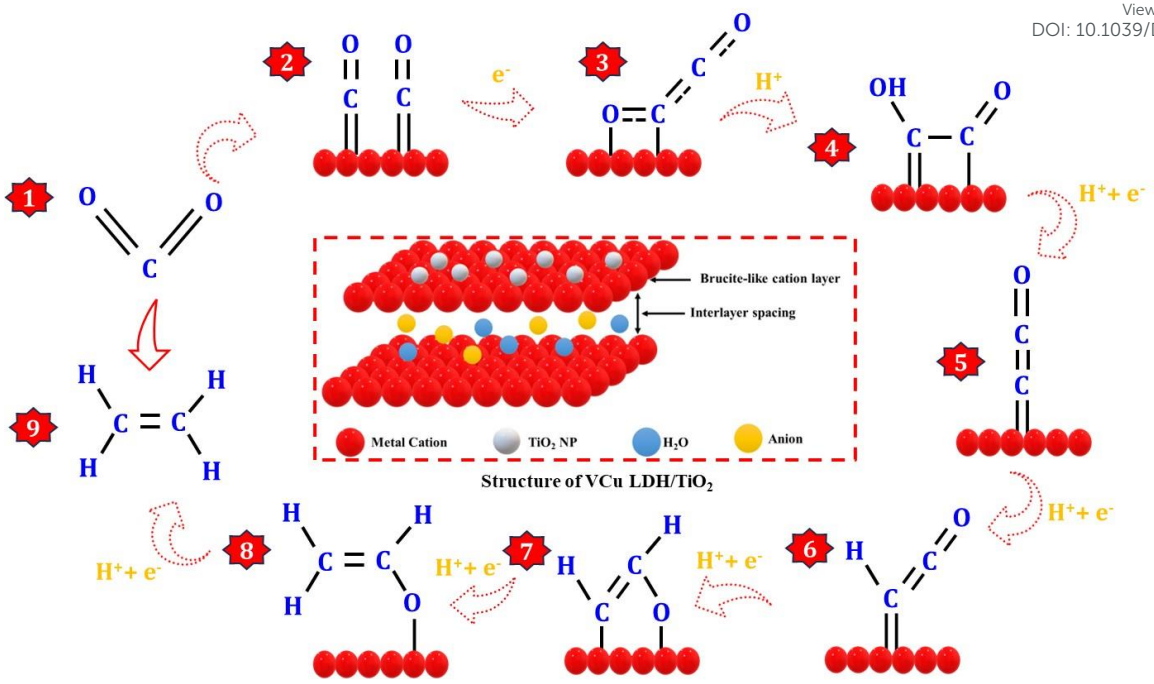

Figure 8: Schematic of CO_2 to ethylene reaction pathway on VCu LDH/TiO_2

The C-C coupling process is pivotal for the formation of C_{2+} products. However, the CO dimerization step is influenced by multiple factors. For example, a high local *CO intermediate coverage brings the reaction intermediates into close proximity on the catalyst surface, facilitating C-C coupling. The atomic configuration and valence state of metals impact the CO adsorption state and bond strength, which can modulate the rate of C-C coupling. The moderate binding strength of two *CO on the metal surface results in C-C coupling, a structure-sensitive reaction that also determines the rate of C_2 product formation [49–51]. In addition to *CO dimerization, several other thermodynamically viable C-C coupling mechanisms have been suggested. These include CHO-CHO, CO-COH, CH_2-CH_2, CH_2-CO, CH_3-$CO_2^{\bullet-}$, and HCHO-HCHO. The active sites and reaction conditions govern the surface concentration of these intermediates and control the primary source of C-C bonds. Following C-C coupling, the subsequent *OCCO hydrodeoxygenation step dictates the selectivity of CO_2RR-to-ethylene [52–57]. The overall reaction for CO_2 to ethylene at cathode and anode can be given as,

at cathode,

$$2CO_2 + 12H^+ + 12e^- \rightarrow C_2H_4 + 4H_2O \qquad \text{(a)}$$

at anode,

$$2H_2O \rightarrow O_2 + 4H^+ + 4e^- \qquad \text{(b)}$$

View Article Online
DOI: 10.1039/D4YA00417E

6. Electrochemical CO_2 Reduction and End-Products Analysis

CO_2RR was carried out in H-cell with 0.1 M $KHCO_3$ electrolyte. Gamry Framework software was used to command for all the electrochemical analysis. Cyclic Voltammetry (CV) was performed, setting voltage window, to perform 10 continuous CV scans from 1 V to -1.5 V (vs. Ag/AgCl) at a scan rate of 500 mV/s in CO_2-saturated 0.1 M $KHCO_3$ to activate the working catalyst. The chronoamperometry was recorded at different potentials as displayed in Figure 9 (a) using potentiostat for CO_2 reduction. Steady state chronoamperometry was performed from -0.1 V to -1.4 V vs RHE. The CV was taken before and after purging CO_2 from 0 V to -1 V vs Ag/AgCl Figure 9 (b). Also, the CV was taken at different scan rates Figure 9 (c) i.e. 20, 40, 60, 80 and 100 mV/sec to calculate double layer capacitance. The Linear Sweep Voltammetry (LSV) was also performed before and after CO_2 purging from 0 V to -2 V vs Ag/AgCl and later converted to RHE Figure 9(d). The current density 40 mA/cm^2 was achieved at ~1.8 V vs RHE. The CV and LSV are not iR-compensated.

Figure 9 (e) is the Electrochemical Impedance Spectroscopy (EIS) taken in the frequency range of 100 kHz to 0.1 Hz using an amplitude of 10 mV AC voltage to determine the resistance of catalyst (R_p) and electrolyte (R_u). The obtained Nyquist plot was fitted using Randle's circuit by Gamry E-chem analyst. VCu LDH/TiO_2 exhibited values of Rp and Ru as 52.27 and 20.99 **Ω** respectively. C_{dl} value Figure 9 (f) is calculated as given in Equation 2,

$$C_{dl} = \Delta J\,(j_a - j_c)/2\gamma \qquad (2)$$

Where,

j_a = anodic current density

j_c = cathodic current density

γ = scan rate in mV/s

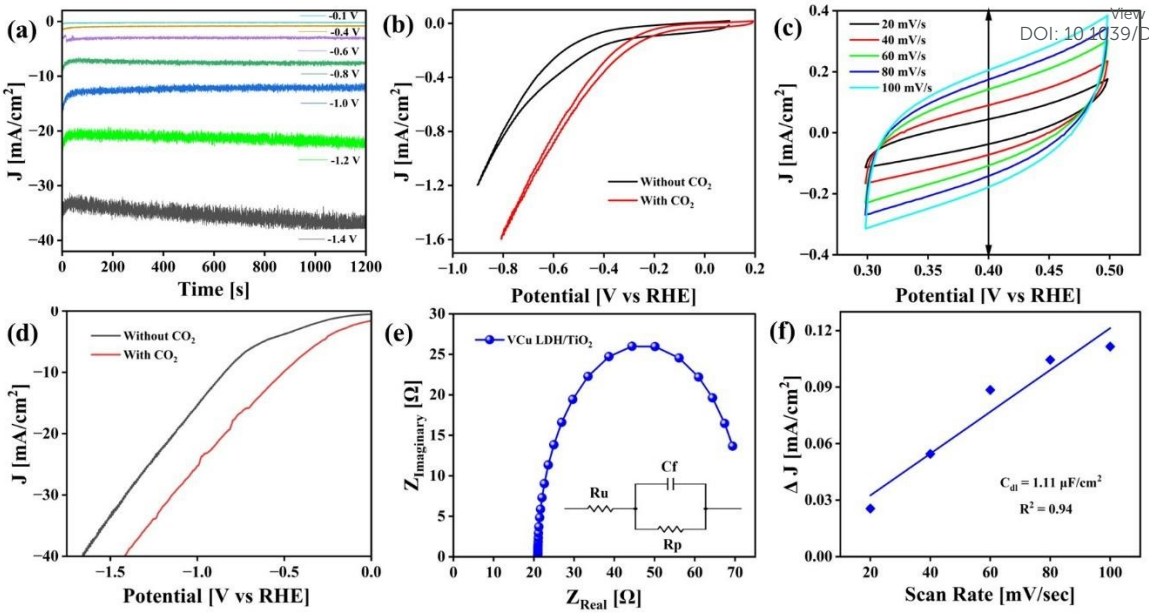

Figure 9: Electrochemical analysis for CO_2RR (a) Chronoamperometry at different potentials, (b) Cyclic voltammetry before and after CO_2 purging, (c) Cyclic voltammetry at different scan rates, (d) Linear Sweep Voltammetry of VCu LDH/TiO_2 before and after CO_2 purging (e) EIS of VCu LDH/TiO_2 and (f) Double layer capacitance calculation plot

An online-GC, equipped with a Porapak-R column and 1 ml sampling loop was used for gas products analysis during CO_2RR. The quantitative analysis of CO and hydrocarbons was done by a Flame Ionization Detector (FID) with a methanizer and H_2 was detected on Thermal Conductivity Detector (TCD). A standard gas mixture was used for the calibration of CO, H_2, CH_4 and C_2H_4 (CO: 1002 ppm; H_2: 1002 ppm, CH_4: 1002 ppm and C_2H_4: 1001 ppm; balanced with Nitrogen). During the electrolysis, CO_2 gas flow rate was maintained at 50.0 sccm, delivering CO_2 into the cathodic compartment containing CO_2-saturated 0.1 M $KHCO_3$ electrolyte, and vented the into GC sampling loop. The voltage was stepwise tuned on working electrode using potentiostat, keeping 20 mins for each potential and recorded the corresponding chronoamperometric curve. The gas products are sampled after a continuous electrolysis of 20 mins under each potential. The 50 sccm CO_2 gas, mixed with continuously produced end products, flowed through the sampling loop (1 mL) of GC during the electrolysis. The CO, CH_4 and C_2H_4 contents were analysed in FID as shown in Figure S4. The final concentrations were obtained by applying calibration method (with above mentioned calibration standards) using Chromatec Navigator. Further calculations for partial current density and faradaic efficiency (SI) as mentioned below in Equation (3) and (4) respectively.

The partial current density (Figure 10 (b)) for a given gas product is calculated as,

$$j_i = x_i \times \vartheta \times \frac{n_i F p_0}{RT} \times (electrode\ area)^{-1} \qquad (3)$$

View Article Online
DOI: 10.1039/D4YA00417E

Where,

x_i = volume fraction of certain end product determined by online GC with reference to calibration curves from standard gas sample,

ϑ = flow rate

n_i = number of electrons involved

p_0 = 101.3 kPa

F = Faradaic constant

R = gas constant

The corresponding FE for each potential (Figure 10 (a, c, d)) is calculated as,

$$FE = {}^{j_i}/_{j_{total}} \times 100\ \% \quad (4)$$

The calculated FEs for CO, H_2, CH_4 and C_2H_4 was displayed in Figure 10 (a, c and d) along with the partial current density plot Figure 10 (b). Some examples of catalysts reported for CO_2RR to ethylene are mentioned in Table 1. The highest FE is obtained at -0.4 V vs RHE along with partial current density of 3.24 mA/cm^2. The Turnover Frequency values (TOF) were obtained for CO, CH_4 and C_2H_4 w.r.t. potential applied during the electrolysis (Supplementary Information). At -0.4 V vs RHE, the TOF was found to be 16.6 (h^{-1}) with catalyst loading of only 0.12 mg/cm^2 (Figure S1). For comparison we have carried out same set of experiments to test the activity of pristine VCu LDH towards CO_2RR and given in Figure S7. The FE values for voth VCu LDH and VCu LDH/TiO2 are shown in Table S1. Using VCu LDH, the FE achieved at -0.4 V RHE was 77.96% which is ~6% lower than the VCu LDH/TiO_2.

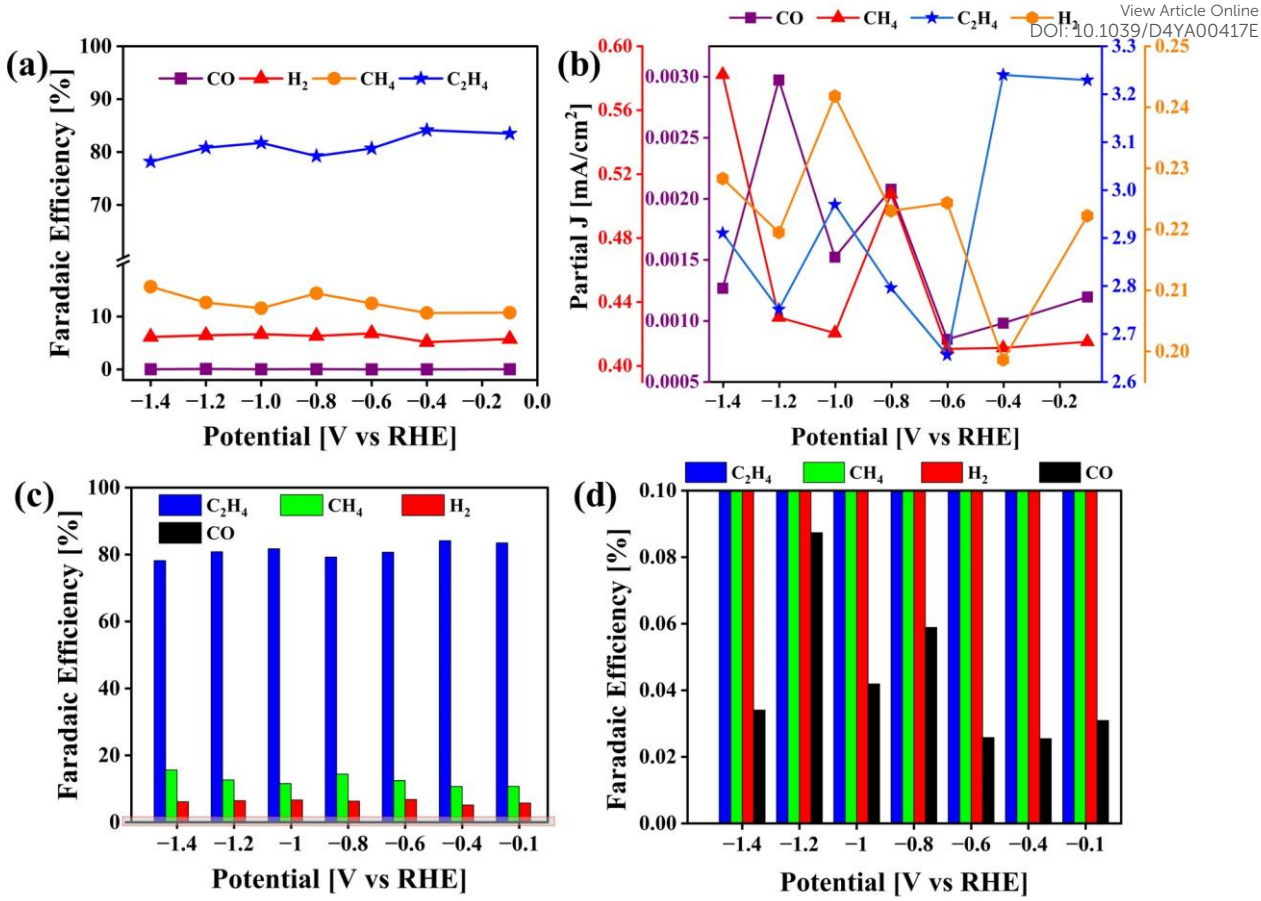

Figure 10: Analysis of CO_2 reduction end products obtained using VCu LDH/TiO_2 catalyst (a) Line + Symbol plot of FEs of CO, H_2, CH_4 and C_2H_4, (b) Line + Symbol plot of Partial Current Densities of CO, H_2, CH_4 and C_2H_4, (c) Bar plot of FEs and (d) Zoom in of (c) bar plot

Table 1: Catalysts reported for CO_2RR to ethylene

Catalyst	Electrolyte	Electrolyser	Faradaic Efficiency (%)	Reference
Carbon-Cu-PTFE	Neutral	Flow cell	70	[58]
Fluorine modified copper	0.1 M $KHCO_3$	Flow cell	80	[59]
Nano dendritic copper catalyst	0.1 M $KHCO_3$	Flow cell	57	[60]
CuAg alloy	1 M KOH	Flow cell	60	[61]
Cu- Polyamine	1 M KOH	Flow cell	72	[62]
Cu nanoparticles on pyridinic-N rich graphene	0.5 M $KHCO_3$	H-Cell	19	[63]

Cu-Zn Alloy	0.1 M $KHCO_3$	H-Cell	33.3	[64]
a-Ni/Cu-NP@CMK	0.1 M $KHCO_3$	Flow cell	72.3	[65]
Ultrathin CuO nanoplate arrays	Neutral KCl	Flow cell	84.5	[66]
Polyamine incorporated Cu electrodes	10 M KOH	Flow cell	87	[67]
Zn-Cu bimetallic GDE	-	H-Cell	40	[68]
MgAl LDH/Cu	1 M $KHCO_3$	Flow cell	55.1	[69]
Electrodeposited Cu	Acidic	Flow cell	60	[70]
VCu LDH/TiO_2	0.1 M $KHCO_3$	H-Cell	84.13	Our work

View Article Online
DOI: 10.1039/D4YA00417E

7. Conclusion

The low cost highly efficient VCu LDH/TiO_2 electrocatalyst was successfully synthesized by hydrothermal process. The X-Ray Diffraction data showed crystalline nature of VCu LDH/TiO_2 electrocatalyst. The uniform flower-like morphology with TiO_2 nanoparticles embedded on the surface of petals was observed from. FESEM. The FT-IR analysis exhibited the vibrational stretching corresponding to formation of LDH material along with the metal peaks rising below 800 cm^{-1}. The porous structure of LDH acting as template for TiO_2 nanoparticles was seen HRTEM. The XPS result showed the existence of elements present in VCu LDH/TiO_2 electrocatalyst and their oxidation states. The strong binding energies of XPS correspond to V^{3+}, Cu^{2+}, Ti^{3+} and O1s. The electrochemical performance CO_2 reduction study shows the formation of value-added end products such as CH_4 and C_2H_4. The LSV data suggest that VCu LDH/TiO_2 reached higher current density at lower voltages. The CO_2 was reduced in traditional H-type cell by utilizing VCu LDH/TiO_2 electrocatalyst into CO, CH_4 and C_2H_4 exhibiting highest FE for C_2H_4 at potential -0.4 V vs RHE. The lowest concentrations of CO (~0) were obtained throughout the range of electrolysis. For C_2H_4, the highest FE was found around 84%. As the potential increases after -0.4 V the corresponding FE for C_2H_4 will reduce and again increase at some interval. The existence of active Cu sites within the VCu LDH/TiO_2 facilitates the generation of the C_2H_4 product. This is attributed to the known propensity of Cu-based materials to yield C_2 products. As the results suggest, potential exists to amplify this process for the purpose of augmenting ethylene production utilizing VCu LDH/TiO_2. The developed electrocatalyst may be utilized for the fabrication of electrode at larger scale and CO_2 electrolyzer as well. The finding of this work suggests that ethylene can be produced at a larger scale via electrochemical conversion of CO_2 and may be effective strategy to achieve net zero as per the Paris agreement of climate change.

8. Supporting Information

The supporting information includes ICP-OES, Electrode preparation, TOF calculations, FESEM, XRD and Gas Chromatography data.

9. Author Information

Corresponding Author

Rohit Srivastava

Email: rohit.s@spt.pdpu.ac.in

View Article Online
DOI: 10.1039/D4YA00417E

ORCID

Sneha S Lavate: 0000-0002-6399-6496

Rohit Srivastava: 0000-0002-9957-8499

10. Author Contribution

Sneha S Lavate: Methodology, Investigation, Validation, Writing-original draft. Rohit Srivastava: Conceptualization, Reviewing, Supervision, Funding acquisition.

11. Funding Sources

This research work was funded by United State India Science and Technology Endowment Fund (USISTEF) (Grant No.: USISTEF/IG-STAGE-I/019/2022).

12. Acknowledgement

Sneha S Lavate and Rohit Srivastava would like to thank Department of Petroleum Engineering, School of Energy Technology, Pandit Deendayal Energy University for providing infrastructure and facilities.

View Article Online
DOI: 10.1039/D4YA00417E

References

[1] D. Higgins, C. Hahn, C. Xiang, T. F. Jaramillo, A. Z. Weber, *ACS Energy Lett.* **2018**, *4*, 317.

[2] L. Yuan, S. Zeng, X. Zhang, X. Ji, S. Zhang, *Mater. Reports Energy* **2023**, *3*, 100177.

[3] S. K. Ray, R. Dahal, M. D. Ashie, B. P. Bastakoti, *Sci. Rep.* **2024**, *14*, 1.

[4] S. K. Ray, R. Dahal, M. D. Ashie, G. Pathiraja, B. P. Bastakoti, *Catal. Sci. Technol.* **2024**, DOI 10.1039/d4cy00270a.

[5] H. Rabiee, L. Ge, X. Zhang, S. Hu, M. Li, Z. Yuan, *Energy Environ. Sci.* **2021**, *14*, 1959.

[6] W. Lv, J. Zhou, J. Bei, R. Zhang, L. Wang, Q. Xu, W. Wang, *Appl. Surf. Sci.* **2017**, *393*, 191.

[7] P. Li, J. Bi, J. Liu, Q. Zhu, C. Chen, X. Sun, J. Zhang, B. Han, *Nat. Commun.* **2022**, *13*, 1.

[8] J. Cai, Q. Zhao, W. Y. Hsu, C. Choi, Y. Liu, J. M. P. Martirez, C. Chen, J. Huang, E. A. Carter, Y. Huang, *J. Am. Chem. Soc.* **2023**, *145*, 9136.

[9] H. Chen, Z. Wang, X. Wei, S. Liu, P. Guo, P. Han, H. Wang, J. Zhang, X. Lu, B. Wei, *Appl. Surf. Sci.* **2021**, *544*, DOI 10.1016/j.apsusc.2021.148965.

[10] D. Karapinar, C. E. Creissen, J. G. Rivera De La Cruz, M. W. Schreiber, M. Fontecave, *ACS Energy Lett.* **2021**, *6*, 694.

[11] R. Srivastava, *Nano-Catalysts for Energy Applications*, CRC Press, Taylor & Francis Group, **2021**.

[12] P. Singh, R. Srivastava, *J. CO2 Util.* **2021**, *53*, 101748.

[13] Y. Wang, J. Liu, G. Zheng, *Adv. Mater.* **2021**, *33*, 2005798.

[14] W. Zhou, K. Cheng, J. Kang, C. Zhou, V. Subramanian, Q. Zhang, Y. Wang, *Chem. Soc. Rev.* **2019**, *48*, 3193.

[15] Z. Zhang, L. Bian, H. Tian, Y. Liu, Y. Bando, Y. Yamauchi, Z. Wang, *Small* **2022**, *18*, 2107450.

[16] J. Qu, X. Cao, L. Gao, J. Li, L. Li, Y. Xie, Y. Zhao, J. Zhang, M. Wu, H. Liu, *Electrochemical Carbon Dioxide Reduction to Ethylene: From Mechanistic Understanding to Catalyst Surface Engineering*, **2023**.

[17] J. Yu, J. Wang, Y. Ma, J. Zhou, Y. Wang, P. Lu, J. Yin, R. Ye, Z. Zhu, Z. Fan, *Adv. Funct. Mater.* **2021**, *31*, 2102151.

[18] L. Fan, C. Xia, F. Yang, J. Wang, H. Wang, Y. Lu, *Sci. Adv.* **2020**, *6*, eaay3111.

[19] G. Wang, J. Chen, Y. Ding, P. Cai, L. Yi, Y. Li, C. Tu, Y. Hou, Z. Wen, L. Dai, *Chem.*

View Article Online
DOI: 10.1039/D4YA00417E

Soc. Rev. **2021**, *50*, 4993.

[20] P. Su, W. Xu, Y. Qiu, T. Zhang, X. Li, H. Zhang, *ChemSusChem* **2018**, *11*, 848.

[21] D. Gao, R. M. Arán-Ais, H. S. Jeon, B. Roldan Cuenya, *Nat. Catal.* **2019**, *2*, 198.

[22] K. Zhao, F. Liu, C. Niu, W. Xu, Y. Dong, L. Zhang, S. Xie, M. Yan, Q. Wei, D. Zhao, L. Mai, *Adv. Sci.* **2015**, *2*, 1.

[23] J. M. Gonçalves, M. Ireno Da Silva, L. Angnes, K. Araki, *J. Mater. Chem. A* **2020**, *8*, 2171.

[24] O. Monfort, P. Petrisková, *Processes* **2021**, *9*, 1.

[25] A. Anzai, M.-H. Liu, K. Ura, T. G. Noguchi, A. Yoshizawa, K. Kato, T. Sugiyama, M. Yamauchi, *Catalysts* **2022**, *12*, DOI 10.3390/catal12050478.

[26] Q. Yang, X. Liu, W. Peng, Y. Zhao, Z. Liu, M. Peng, Y. R. Lu, T. S. Chan, X. Xu, Y. Tan, *J. Mater. Chem. A* **2021**, *9*, 3044.

[27] G. K. Ramesha, J. F. Brennecke, P. V. Kamat, *ACS Catal.* **2014**, *4*, 3249.

[28] H. He, P. Zapol, L. A. Curtiss, *J. Phys. Chem. C* **2010**, *114*, 21474.

[29] L. Mohapatra, K. M. Parida, K. Parida, **2016**.

[30] S. Lokesh, R. Srivastava, *Energy & Fuels* **2022**, *36*, 13417.

[31] S. Lokesh, R. Srivastava, *Int. J. Hydrogen Energy* **2023**, *48*, 35.

[32] S. Kawamura, M. C. Puscasu, Y. Yoshida, Y. Izumi, G. Carja, *Appl. Catal. A Gen.* **2015**, *504*, 238.

[33] R. Gao, J. Zhu, D. Yan, *Nanoscale* **2021**, *13*, 13593.

[34] Z. Guo, W. Ye, X. Fang, J. Wan, Y. Ye, Y. Dong, **2019**.

[35] A. L. Johnston, E. Lester, O. Williams, R. L. Gomes, *J. Environ. Chem. Eng.* **2021**, *9*, 105197.

[36] D. Panchal, A. Sharma, P. Mondal, O. Prakash, S. Pal, *Appl. Surf. Sci.* **2021**, *553*, 149577.

[37] Y. Zhao, H. Lin, M. Chen, D. Yan, *Ind. Eng. Chem. Res.* **2014**, *53*, 3140.

[38] S. Guru, S. Kumar, S. Bellamkonda, R. R. Gangavarapu, *Int. J. Hydrogen Energy* **2021**, *46*, 16414.

[39] S. S. Lavate, R. Srivastava, *ChemSusChem* **2024**, *n/a*, e202400774.

[40] C. Wang, M. Cao, P. Wang, Y. Ao, J. Hou, J. Qian, *Appl. Catal. A Gen.* **2014**, *473*, 83.

[41] L. Wang, X. Gao, Y. Cheng, X. Zhang, G. Wang, Q. Zhang, J. Su, *J. Photochem. Photobiol. A Chem.* **2019**, *369*, 44.

[42] Z. Zhang, L. Bian, H. Tian, Y. Liu, Y. Bando, Y. Yamauchi, Z. L. Wang, *Small* **2022**, *18*, DOI 10.1002/smll.202107450.

[43] J. Li, Z. Wang, C. McCallum, Y. Xu, F. Li, Y. Wang, C. M. Gabardo, C.-T. Dinh, T. T. Zhuang, L. Wang, *Nat. Catal.* **2019**, *2*, 1124.

[44] C. M. Gunathunge, V. J. Ovalle, Y. Li, M. J. Janik, M. M. Waegele, *ACS Catal.* **2018**, *8*, 7507.

[45] E. Pérez-Gallent, M. C. Figueiredo, F. Calle-Vallejo, M. T. M. Koper, *Angew. Chemie Int. Ed.* **2017**, *56*, 3621.

[46] C. Choi, S. Kwon, T. Cheng, M. Xu, P. Tieu, C. Lee, J. Cai, H. M. Lee, X. Pan, X. Duan, *Nat. Catal.* **2020**, *3*, 804.

[47] Y. Zhou, F. Che, M. Liu, C. Zou, Z. Liang, P. De Luna, H. Yuan, J. Li, Z. Wang, H. Xie, *Nat. Chem.* **2018**, *10*, 974.

[48] F. Li, A. Thevenon, A. Rosas-Hernández, Z. Wang, Y. Li, C. M. Gabardo, A. Ozden, C. T. Dinh, J. Li, Y. Wang, *Nature* **2020**, *577*, 509.

[49] T.-C. Chou, C.-C. Chang, H.-L. Yu, W.-Y. Yu, C.-L. Dong, J.-J. Velasco-Vélez, C.-H. Chuang, L.-C. Chen, J.-F. Lee, J.-M. Chen, *J. Am. Chem. Soc.* **2020**, *142*, 2857.

[50] S. Nitopi, E. Bertheussen, S. B. Scott, X. Liu, A. K. Engstfeld, S. Horch, B. Seger, I. E. L. Stephens, K. Chan, C. Hahn, *Chem. Rev.* **2019**, *119*, 7610.

[51] S. Xie, W. Ma, X. Wu, H. Zhang, Q. Zhang, Y. Wang, Y. Wang, *Energy Environ. Sci.* **2021**, *14*, 37.

[52] A. A. Peterson, F. Abild-Pedersen, F. Studt, J. Rossmeisl, J. K. Nørskov, *Energy Environ. Sci.* **2010**, *3*, 1311.

[53] X. Sun, Q. Zhu, X. Kang, H. Liu, Q. Qian, J. Ma, Z. Zhang, G. Yang, B. Han, *Green Chem.* **2017**, *19*, 2086.

[54] H. Xiao, T. Cheng, W. A. Goddard III, R. Sundararaman, *J. Am. Chem. Soc.* **2016**, *138*, 483.

[55] X. Nie, M. R. Esopi, M. J. Janik, A. Asthagiri, *Angew. Chemie Int. Ed.* **2013**, *52*.

[56] S. Ma, M. Sadakiyo, R. Luo, M. Heima, M. Yamauchi, P. J. A. Kenis, *J. Power Sources* **2016**, *301*, 219.

[57] C. Genovese, C. Ampelli, S. Perathoner, G. Centi, *Green Chem.* **2017**, *19*, 2406.

[58] Z. Wang, Y. Li, X. Zhao, S. Chen, Q. Nian, X. Luo, J. Fan, D. Ruan, B. Q. Xiong, X. Ren, *J. Am. Chem. Soc.* **2023**, *145*, 6339.

[59] W. Ma, S. Xie, T. Liu, Q. Fan, J. Ye, F. Sun, Z. Jiang, Q. Zhang, J. Cheng, Y. Wang, *Nat. Catal.* **2020**, *3*, 478.

[60] C. Reller, R. Krause, E. Volkova, B. Schmid, S. Neubauer, A. Rucki, M. Schuster, G. Schmid, *Adv. Energy Mater.* **2017**, *7*, 1602114.

View Article Online
DOI: 10.1039/D4YA00417E

[61] T. T. H. Hoang, S. Verma, S. Ma, T. T. Fister, J. Timoshenko, A. I. Frenkel, P. J. A. Kenis, A. A. Gewirth, *J. Am. Chem. Soc.* **2018**, *140*, 5791.

[62] X. Chen, J. Chen, N. M. Alghoraibi, D. A. Henckel, R. Zhang, U. O. Nwabara, K. E. Madsen, P. J. A. Kenis, S. C. Zimmerman, A. A. Gewirth, *Nat. Catal.* **2021**, *4*, 20.

[63] Q. Li, W. Zhu, J. Fu, H. Zhang, G. Wu, S. Sun, *Nano Energy* **2016**, *24*, 1.

[64] Y. Feng, Z. Li, H. Liu, C. Dong, J. Wang, S. A. Kulinich, X. Du, *Langmuir* **2018**, *34*, 13544.

[65] B. Chen, L. Gong, N. Li, H. Pan, Y. Liu, K. Wang, J. Jiang, *Adv. Funct. Mater.* **2024**, *34*, 2310029.

[66] J. Yuan, J. J. Zhang, M. P. Yang, W. J. Meng, H. Wang, J. X. Lu, *Catalysts* **2018**, *8*, DOI 10.3390/catal8040171.

[67] X. Chen, J. Chen, N. M. Alghoraibi, D. A. Henckel, R. Zhang, U. O. Nwabara, K. E. Madsen, P. J. A. Kenis, S. C. Zimmerman, A. A. Gewirth, *Nat. Catal.* **2021**, *4*, 20.

[68] M. H. Suliman, H. Al Naji, M. Usman, *Electrochim. Acta* **2024**, *500*, 144723.

[69] Y. N. Xu, W. Li, H. Q. Fu, X. Y. Zhang, J. Y. Zhao, X. Wu, H. Y. Yuan, M. Zhu, S. Dai, P. F. Liu, *Angew. Chemie* **2023**, *135*, e202217296.

[70] Y. Cao, Z. Chen, P. Li, A. Ozden, P. Ou, W. Ni, J. Abed, E. Shirzadi, J. Zhang, D. Sinton, J. Ge, E. H. Sargent, *Nat. Commun.* **2023**, *14*, DOI 10.1038/s41467-023-37898-8.

View Article Online
DOI: 10.1039/D4YA00417E

Data Availability Statement

The data supporting this article have been included as part of the Supplementary Information.